

## 1. AFOSR award # and name of the recipient (Institution)

FA9550-09-1-0133, The Virginia Polytechnic Institute and State University

## 2. Project Title and name of the PI

Shashank Priya

(YIP 09) DOMAIN ENGINEERED MAGNETOELECTRIC THIN FILMS FOR HIGH SENSITIVITY RESONANT MAGNETIC FIELD SENSORS

## 3. Date of the report and period covered by the report

January 2009 – December 2011

## 4. Description of the Research Progress

### 4.1 Ferroelectric thin film synthesis and texture analysis

Sol-gel deposition and RF sputtering process was developed for deposition of PZT on Pt/Ti/SiO<sub>2</sub>/Si (hereafter, referred to as platinized Si) substrates as shown in Fig. 1. Target preparation was perfected for Zr/Ti ratios of 60/40 and 52/48 with excess Pb to compensate for Pb loss during post deposition annealing. As deposited PZT RF (henceforth, RF refers to “RF sputtering” in this report) thin films were not well textured (i.e. with preferred crystalline orientation). To texture and obtain crack-free thick PZT RF films, we employed pre-treated substrates and post-deposition annealing. One pre-treatment was the use of seed layer of textured PZT sol-gel thin film of thickness 65-85nm [1].

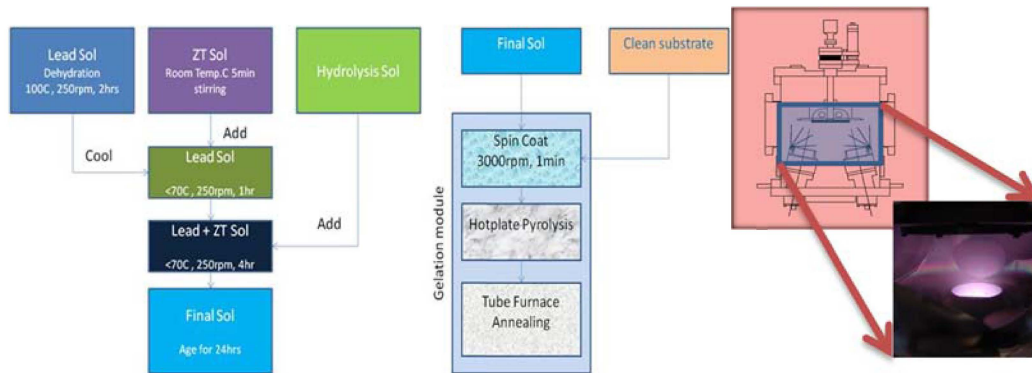


**Figure 1:** Sol-gel process flow and the RF sputter configuration for deposition of PZT thin films.

A detailed study was conducted to determine the conditions for obtaining preferred crystallite orientations (referred as textured). The results of this study were summarized in Temperature-Time-Transformation (TTT) diagrams. These diagrams provide two-dimensional relationships of crystalline orientation to pyrolysis and annealing conditions. To augment our understanding of the thermal budgets required for the texturing of the PZT sol-gel thin films, we further developed relationships between each phase and the experimental conditions. In addition, the optical band gap, morphology and composition of highly textured sol-gel thin films were evaluated using Variable Angle Spectroscopic Ellipsometry (VASE), Raman scattering, piezoresponse force microscopy (PFM) and X-ray photoelectron spectroscopy (XPS). RF sputter deposition operating space was explored using statistically designed experiments (using Design Expert software) and ANOVA (Analysis of Variance) models were formulated. The responses were thickness, refractive index and absorption coefficient from ellipsometric data and the elemental compositions from energy dispersive X-ray

analysis of the PZT thin films. These models were then utilized to predict and optimize the process conditions necessary to obtain the preferred responses.

Temperature-Time-Transformation model for sol-gel deposited PZT (60/40) films: We conducted detailed investigation on the texture evolution as this will directly influence the electrical response of the high frequency sensor structure. Based on our statistically designed experiments the two parameters, annealing temperature and time, were more significant than the pyrolysis conditions in achieving proper texture. This is clearly evident in the half normal probability plots of the Effects (measure of the process variable's influence on the response) shown in Fig. 2. The responses were normalized XRD peak heights for [100], [110] and [111] orientations at 2-theta angles of 22°, 31° and 39° respectively.

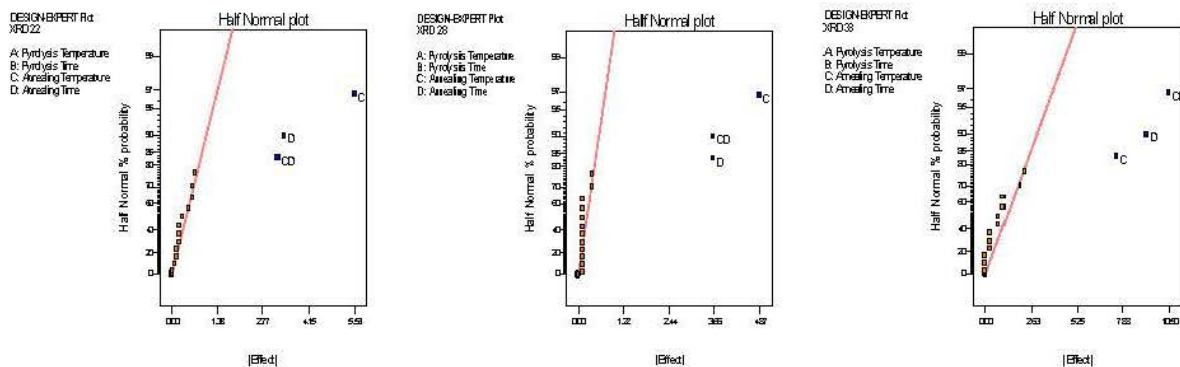


**Figure 2:** Half normal probability plots of XRD responses – [100], [110] and [111] peak heights.

Based on this information, further extensive exploration of the sol-gel thermal budget operating space was conducted. These experiments are summarized in Temperature-Time-Transformation (TTT) diagrams shown in Fig. 3. This is similar to the diagram that was reported by Chen and Chen [2] except that their main process variables were pyrolysis temperature and time and they had maintained constant annealing temperature and time. However, we wanted to expand beyond these pictorial guides and decided to develop mathematical relationships between XRD peak data and thermal processing conditions. The data utilized to create the TTT diagrams were analyzed using JMP statistical software and the quadratic fits are shown in Fig. 4. Despite moderate  $R^2$  values, the predictability of the quadratic model was found to be poor. A good hint towards this unpredictability can be witnessed in the portion of points that do not trend with the surface plots. The main reason for this poor fit was that we did not take into account proportionality between different crystalline orientations (see Scatter plot matrix correlation in Figure 5).

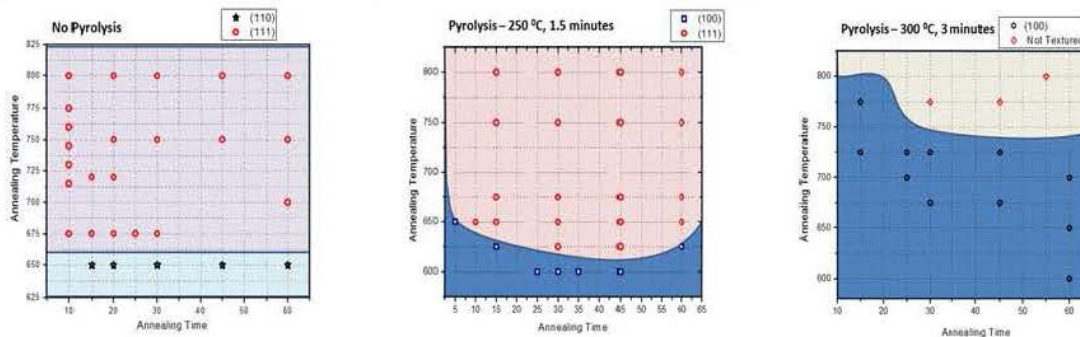


**Figure 3:** Temperature-Time-Transformation diagrams of PZT sol-gel thin films pyrolyzed at a) No pyrolysis, b) 250°C, 1.5 minutes, and c) 300°C, 3 minutes.

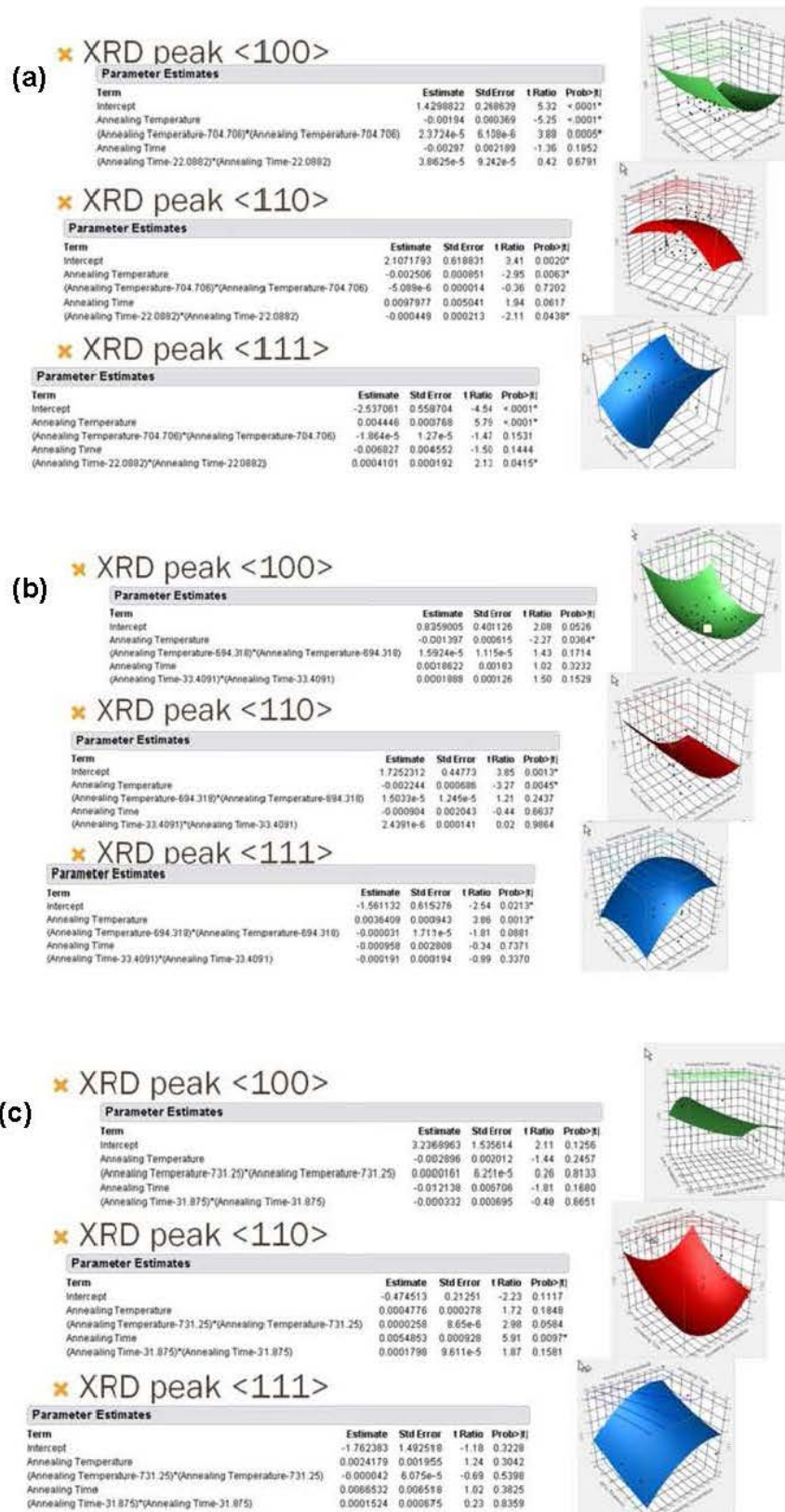
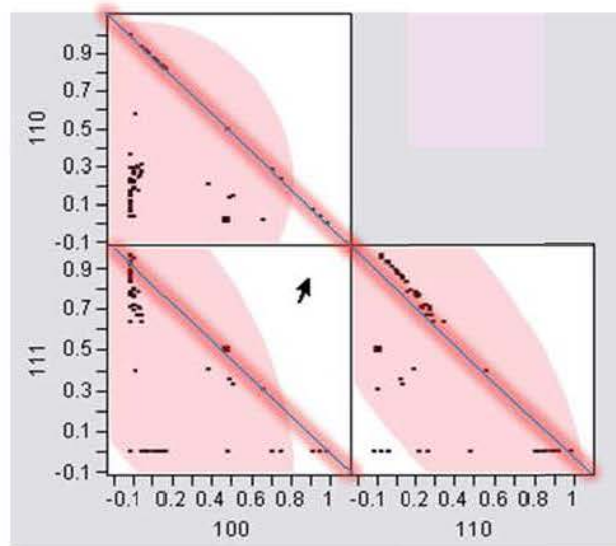


Figure 4: JMP contour plots of PZT sol-gel thin films pyrolyzed at: a) none, b) 250°C for 1.5min, and c) 300°C for 3min, prior to annealing.



**Figure 5:** Scatter plot matrix of the responses (XRD peak data).

We next utilized Logistic regression of the XRD peak data against the 3 process variables - pyrolysis temperature/time, annealing temperature and annealing time. We lumped the pyrolysis variables of temperature and time together as they were blocked experiments with both variant between the blocks. We therefore in statistical terms made pyrolysis temperature/time as categorical variables. The normalized XRD peak data response for three different crystalline orientations of [100], [110] and [111] were easily converted to proportions. The final statistical responses were probabilities of occurrence of each orientation in a particular thin film sample at the stipulated thermal conditions. These probabilities are legit transformation of the unordered proportions of [100], [110] and [111]. These responses were modeled against a linear predictor model of the thermal categorical and continuous factors. Unlike pyrolysis variables which were fixed as categorical, we attempted both continuous and categorical versions of the annealing temperature and time variables.

$$Probability[100] = 1 / (1 + \text{Exp}(-\text{Lin}[100]) + \text{Exp}(\text{Lin}[110] - \text{Lin}[100]))$$

$$Probability[110] = 1 / (1 + \text{Exp}(\text{Lin}[100] - \text{Lin}[110]) + \text{Exp}(-\text{Lin}[110]))$$

$$Probability[111] = 1 / (1 + \text{Exp}(\text{Lin}[100]) + \text{Exp}(\text{Lin}[110]))$$

$$= 1 - Probability[110] - Probability[100]$$

For categorical predictor factors,

$$\text{Lin}[xxx] = \text{Intercept} + \text{function of (pyrolysis time, annealing temperature, pyrolysis time*annealing temperature, annealing time, pyrolysis time*annealing time)}$$

For continuous predictor factors,

$$\text{Lin}[xxx] = \text{Intercept} + \text{function of (pyrolysis time, annealing temperature, pyrolysis time*annealing temperature, annealing time, pyrolysis time*annealing time, annealing time)}$$

*temperature\*annealing time, pyrolysis time\*annealing temperature\*annealing time)*

For prediction when using categorical predictor factors, only annealing factor values used in model were permitted whilst for continuous predictor factors any annealing factor values within range were permitted. We created 4 samples shown in Table 1, SG1, SG2, RV1 and RV2 where SG and RV refers to PZT sol mixed up by two different operators but each at four different pyrolysis and annealing conditions.

**Table 1:** XRD normalized data vs. model predictions for four different samples.

Sample	Categories	Actual	Categorical Model	Continuous Model
SG1	[100]	0.88	0.924	0.878
	[110]	0.12	0.076	0.0417
	[111]	0	4.29E-06	0.08
SG2	[100]	0.896	0.924	0.878
	[110]	0.104	0.076	0.0417
	[111]	0	4.29E-06	0.08
RV1	[100]	0.91	0.924	0.878
	[110]	0.09	0.076	0.0417
	[111]	0	4.29E-06	0.08
RV2	[100]	0.042	0	0
	[110]	0.083	0.022	0.034
	[111]	0.875	0.978	0.966

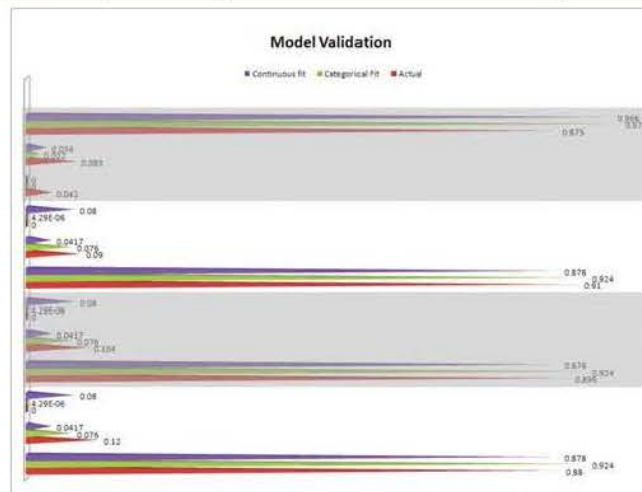


**Figure 6:** Comparison of prediction results for four sol-gel samples shown in Table 1 – red is Actual, Green is Categorical and Purple is Continuous fit.

We observed that the data utilized to create the Temperature-Time-Transformation (TTT) diagrams do not follow any simple multiple regression (like linear or multi order polynomial; Figure 7)) trends. The reason

being that material textured in one phase or orientation will have lesser proportion of the other phases or orientation. For example, PZT 52/48 has three dominant textures, <100>, <110> and <111> and therefore the TTT data for such a system is trinomial and interdependent (Figure 8).

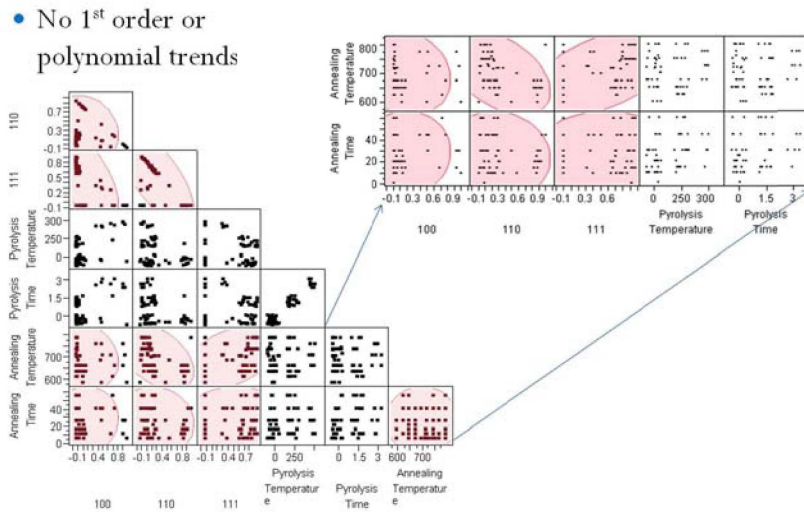


**Figure 7:** Scatter plot matrix showing the lack of a linear or higher order trends between PZT crystalline orientations and TTT conditions.

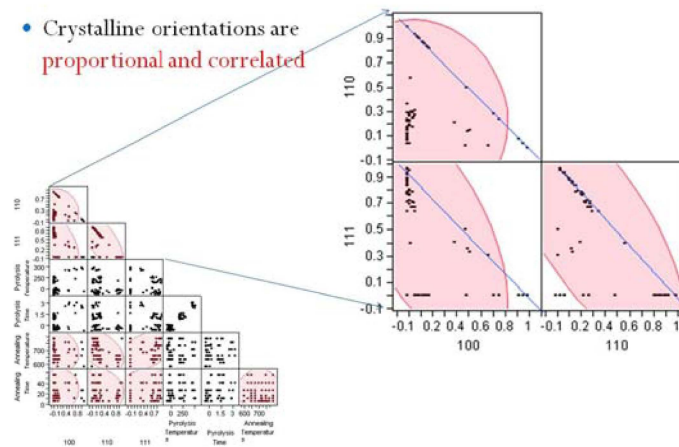


**Figure 8:** Scatter plot matrix of the responses (XRD peak data).

We utilized two multivariate regression approaches, multinomial logistic and log ratio multivariate regressions of the XRD peak data against the 3 process variables - Pyrolysis Temperature/Time and Annealing Temperature and Time. The constitutive equations are given below.

$$Lin[100] = \ln \left( \frac{p_{[100]}}{p_{[111]}} \right) = X\alpha$$

$$Lin[110] = \ln \left( \frac{p_{[110]}}{p_{[111]}} \right) = X\beta$$

$$p_{[100]} = (1 + \exp(-Lin[100]) + \exp(Lin[110] - Lin[100]))^{-1}$$

$$p_{[110]} = (1 + \exp(-\text{Lin}[110]) + \exp(\text{Lin}[100] - \text{Lin}[110]))^{-1}$$

$$p_{[111]} = (1 + \exp(\text{Lin}[100]) + \exp(\text{Lin}[110]))^{-1}$$

$$LR1 = \ln\left(\frac{[100]}{[111]}\right)$$

$$LR2 = \ln\left(\frac{[110]}{[111]}\right)$$

$$[100] = (1 + \exp(-LR1) + \exp(LR2 - LR1))^{-1}$$

$$[110] = (1 + \exp(-LR2) + \exp(LR1 - LR2))^{-1}$$

$$[111] = (1 + \exp(LR1) + \exp(LR2))^{-1}$$

For Categorical Predictor Factors,

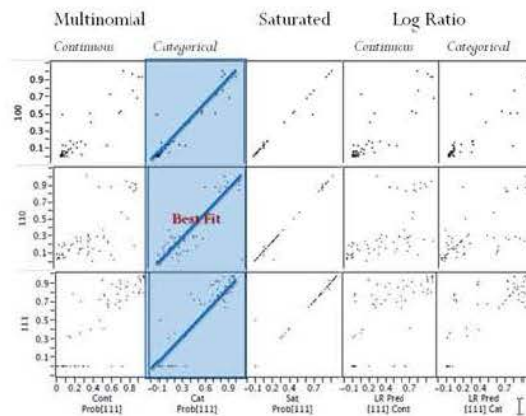
$$X\alpha = \alpha_0 + \alpha_P P + \alpha_{Tm} Tm + \alpha_{P*Tm} P * Tm + \alpha_{P*Tp} P * Tp + \alpha_{Tp} Tp$$

$$X\beta = \beta_0 + \beta_P P + \beta_{Tm} Tm + \beta_{P*Tm} P * Tm + \beta_{P*Tp} P * Tp + \beta_{Tp} Tp$$

For Continuous Predictor Factors,

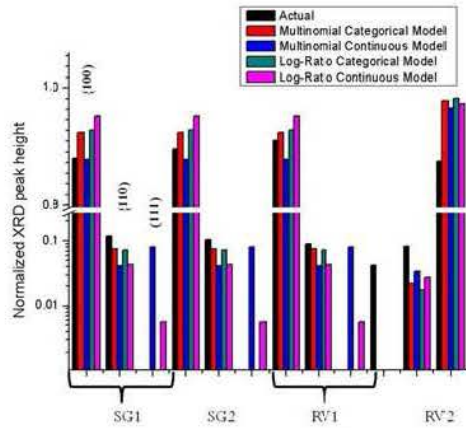
$$X\alpha = \alpha_0 + \alpha_P P + \alpha_{Tm} Tm + \alpha_{P*Tm} P * Tm + \alpha_{P*Tp} P * Tp + \alpha_{Tp} Tp + \alpha_{Tm*Tp} Tm * Tp + \alpha_{P*Tm*Tp} P * Tm * Tp$$

$$X\beta = \beta_0 + \beta_P P + \beta_{Tm} Tm + \beta_{P*Tm} P * Tm + \beta_{P*Tp} P * Tp + \beta_{Tp} Tp + \beta_{Tm*Tp} Tm * Tp + \beta_{P*Tm*Tp} P * Tm * Tp$$



**Figure 9:** Multivariate regression fits to TTT data.

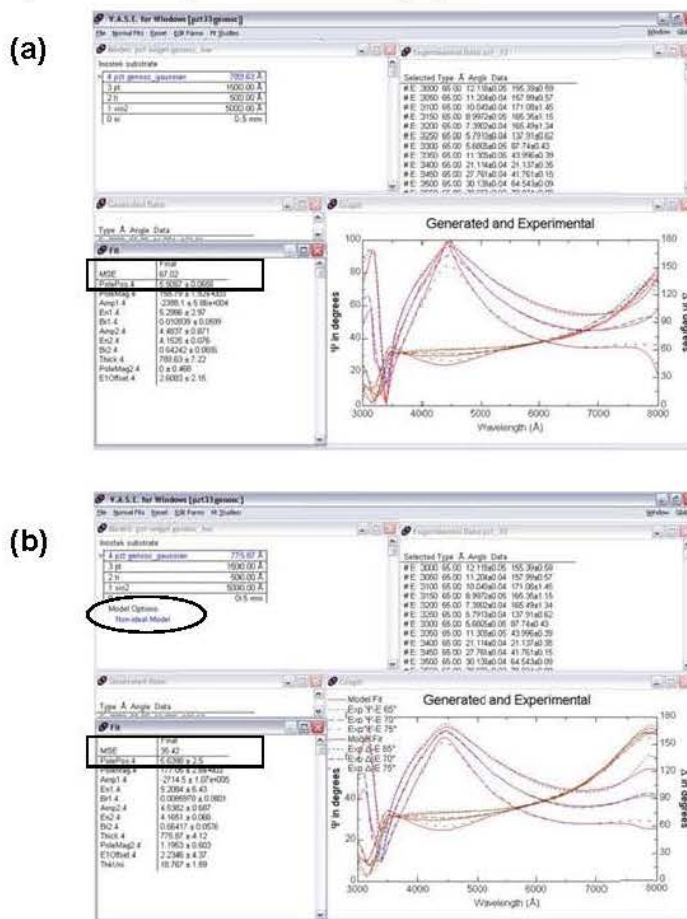
From Figure 9, we observe that multinomial categorical gave the best fit to the TTT data. For model validation, we created 4 samples, SG1, SG2, RV1 and RV2 and the model predictions from multinomial categorical approach was confirmed as the best (Figure 10).



**Figure 10:** Comparison of prediction results for 4 sol-gel samples shown in Table 1 – red is Actual, Green is Categorical and Purple is Continuous fit.

#### 4.2 Interfacial and structural studies of textured PZT sol-gel samples

Initially commonly used VASE analysis was utilized to study the PZT sol-gel films on platinized Si substrates. But the analysis was complicated by poor fit between the model and data (mean square error values in Fig. 11). Film inhomogeneities were accounted in the model and better fits were obtained by utilizing optical non-idealities (non-uniformity in measurement spot).



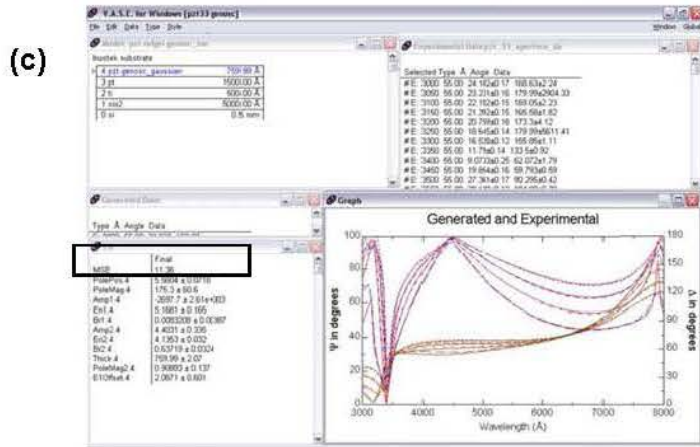


**Figure 11:** VASE modeling issues on PZT sol-gel thin films: (a) as-is MSE of 67.02, (b) MSE of 35.42 with non-ideal modeling, and (c) MSE of 11.36 with aperture.

However, further investigation revealed that as VASE measurement setup utilizes an optical beam incident at an angle to the surface (Fig. 12), we were sampling the edge bead (see Fig. 12) of the spin coated sol-gel films and excluding this non-uniform film around the sample edges, lead to better fits. The fix was the combination of lower angle of incidence, use of an aperture as shown in Fig. 13 and higher data averaging.

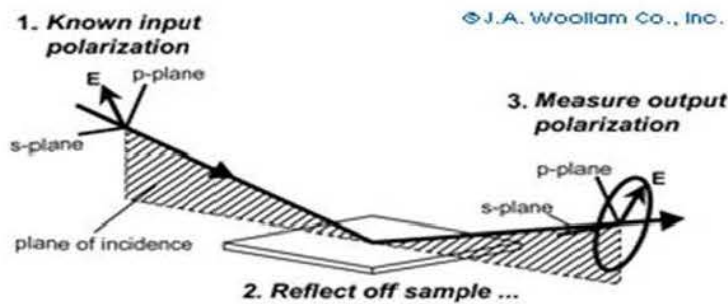


**Figure 12:** Angle of incidence of assaying light in VASE.

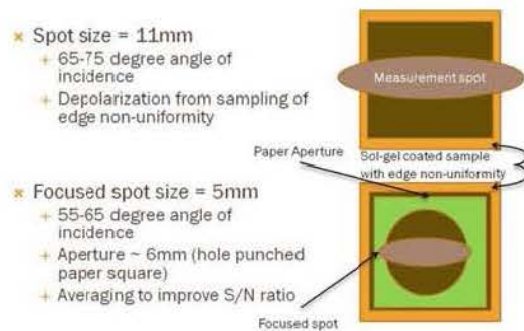


**Figure 13:** Use of an aperture resolved the lack of fit issues.

To understand the effect of substrate on heterogeneous nucleation of PZT sol-gel thin films, we conducted depth profiling using incremental Ar sputtering followed by X-ray photoelectron spectroscopy as shown in Fig. 14. We observed an artifact of the XPS depth profiles (knock-on effect), that is there was an unnatural large gradient of elemental concentrations at the interface between the PZT film and platinum under layer. In an

85nm PZT thin film, 20-30 nm of grading would be easily discriminated by the VASE analysis and therefore this gradient was unreal.

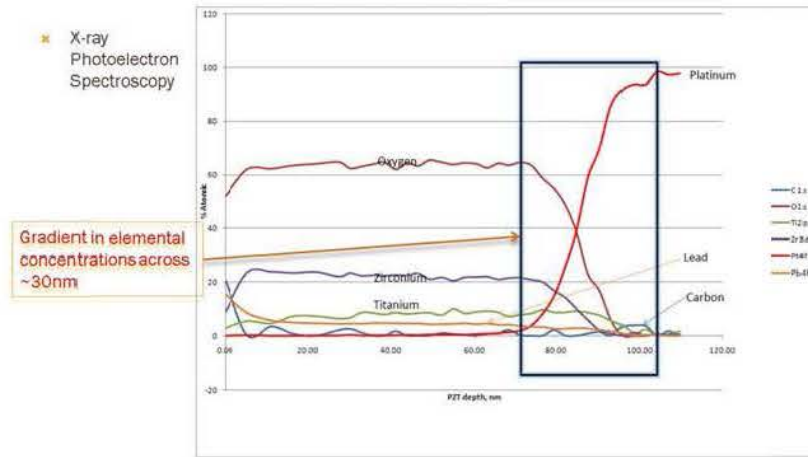


**Figure 14:** XPS depth profile of PZT sol-gel sample.

We conducted the AFM analysis of the sputtered crater as shown in Fig. 15 and found 20-30nm roughness that obliterates any sharp transition at the PZT and Pt interface. High resolution binding energy XPS depth profile scans shown in Fig. 16 were then attempted and we were unable to discern any interfacial heterogeneity.

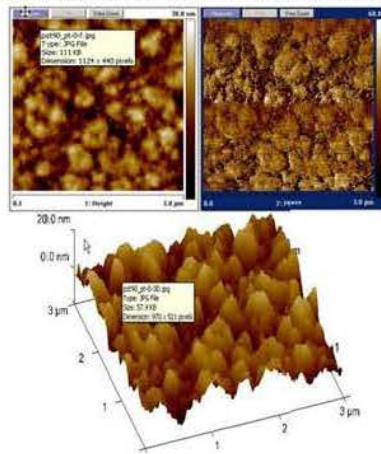


**Figure 15:** 20nm roughness at PZT-Pt interface in sputtered crater of the XPS depth profiled sol-gel sample.

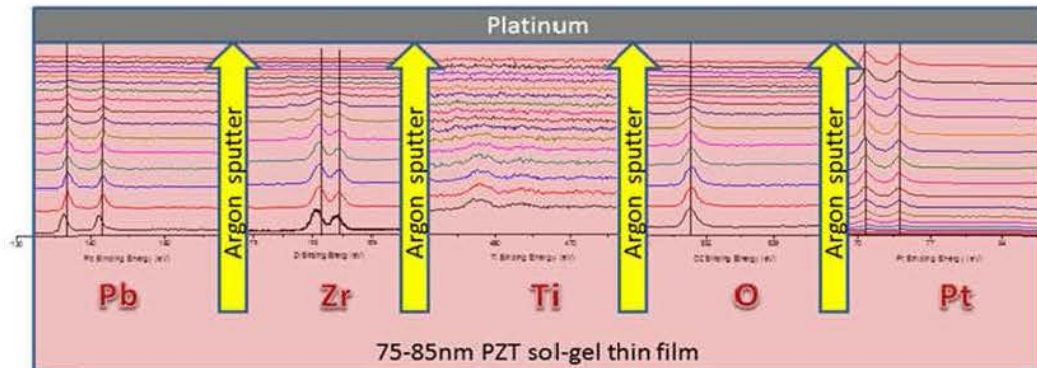


**Figure 16:** High resolution binding energy XPS depth profiling of PZT sol-gel thin film.

Ellipsometric data can be used to determine the optical band gap of highly textured PZT thin films using a Tauc plot (Fig. 17) for direct band gap material where  $\alpha = \frac{4\pi k}{\lambda}$  is computed from absorption coefficient (k) and its square is plotted against incident light energy [3]. The x-axis intercept of the tangent to the sloped line beyond the absorption edge gives us the optical band gap  $E_g$ . We see the  $E_g$  trends as (111) > (100) > (110). The triangular area between the Tauc curve and the tangent is a measure of the sub-band gap density of trap states and this trend was found to be: (110) > (111) > (100).

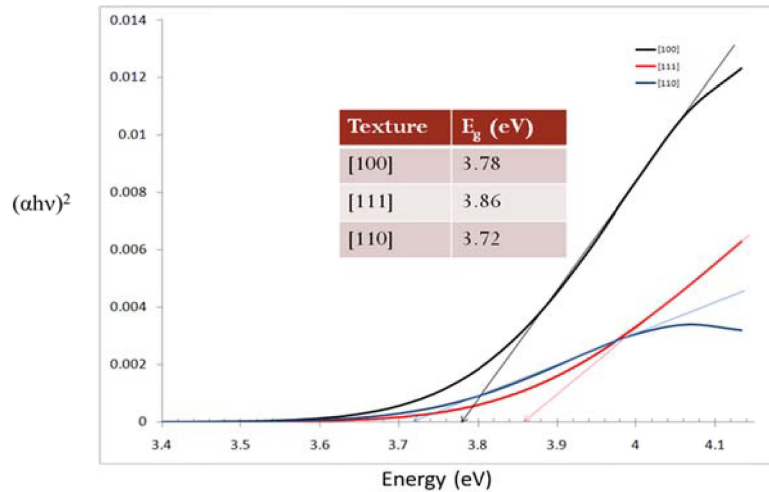


**Figure 17:** Tauc's plot to determine the optical band gap of highly textured PZT thin films.

The deposition process variables were – argon and oxygen flows, chamber pressure, RF power (DC Bias), working distance, temperature, rotation speed and substrate bias. A statistically designed experiment (SDE/DOE) for 8 variables will consist of  $2^8 = 256$  runs (# of runs =  $2^n$  where n is # of variables). This experimentation is best conducted in one session to limit the variance and such a large number of runs will require considerable sample preparation and time allocation. So it is best advised to decrease the number of variables or combine them in the first screening experiment. We combined  $O_2$  and Ar into varying  $O_2$  flow in a fixed Ar flow, fixed working distance and rotation speed and blocked for substrate temperature at two settings of room temperature and  $100^\circ C$ . In doing so, we reduced the experiment to  $2^4 = 16$  runs + 2 temperature blocks + 2 center runs per block = TOTAL of 18 experiments (Table 2).

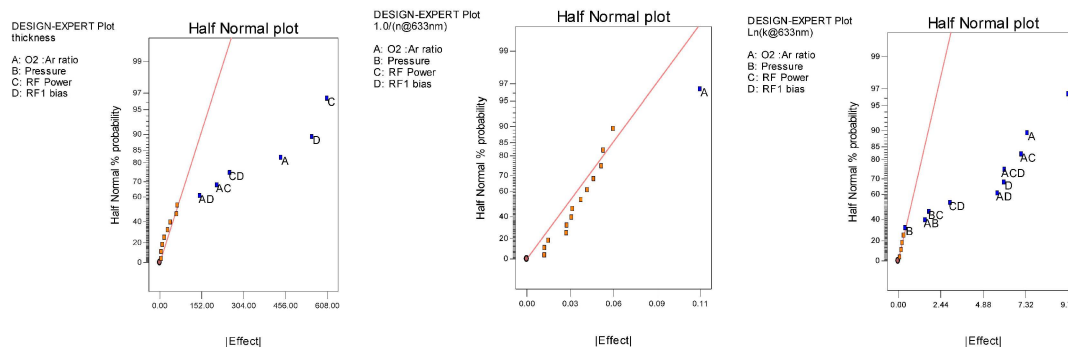


**Figure 18:** Half normal probability plots of VASE responses – thickness, refractive index and absorption coefficient.

**Table 2:** Full factorial statistical design of experiment in four process variables and the measured VASE responses.

Std	Run	Block	Factor 1 A:Ar:O2 ratio	Factor 2 B:Pressure mT	Factor 3 C:RF Power W	Factor 4 D:RF1 bias W	Response 1 thickness A	Response 2 n@633nm	Response 3 k@633nm
8	1	High Temperature	4.00	7.00	200.00	0.00	761.92	1.7856	0.0038439
14	2	High Temperature	4.00	3.00	200.00	10.00	399.17	1.8497	0.013923
5	3	High Temperature	2.00	3.00	200.00	0.00	1306.32	2.2545	2.052E-005
9	4	High Temperature	2.00	3.00	100.00	10.00	376.88	2.0173	0.018048
15	5	High Temperature	2.00	7.00	200.00	10.00	662.98	1.9565	1.6201E-010
3	6	High Temperature	2.00	7.00	100.00	0.00	666.47	2.2757	0.34823
17	7	High Temperature	3.00	5.00	150.00	5.00	393.99	1.6314	0.012359
2	8	High Temperature	4.00	3.00	100.00	0.00	471.82	1.8707	0.096903
12	9	High Temperature	4.00	7.00	100.00	10.00	No deposition		
18	10	Room Temperature	3.00	5.00	150.00	5.00	426.24	1.8802	0.021286
16	11	Room Temperature	4.00	7.00	200.00	10.00	442.44	1.9399	0.026216
4	12	Room Temperature	4.00	7.00	100.00	0.00	394.42	1.6124	0.033182
6	13	Room Temperature	4.00	3.00	200.00	0.00	951.25	2.0639	0.016531
11	14	Room Temperature	2.00	7.00	100.00	10.00	355.04	1.7938	0.0061854
10	15	Room Temperature	4.00	3.00	100.00	10.00	No deposition		
13	16	Room Temperature	2.00	3.00	200.00	10.00	758.56	2.0214	1.4639E-011
7	17	Room Temperature	2.00	7.00	200.00	0.00	1369.34	2.1445	0.00062518
1	18	Room Temperature	2.00	3.00	100.00	0.00	564.84	2.5352	0.57916

The responses were VASE measured thin film parameters – thickness, refractive index (n @ 633nm) and absorption coefficient (k @633nm). Despite having two thin film deposition runs being immeasurable, the significant factors were easily decipherable as shown in the Half Normal Probability plots in Fig. 18. The results of the analysis of variance of VASE data gave us the following models for responses (refractive index and absorption coefficient were transformed for more linearity in the model).

$$\text{Thickness} = -158.01581 + 906.09265 * \text{O2 :Ar ratio} + 7.51601 * \text{RF Power} + 21.59485 * \text{RF1 bias} - 14.30249 * \text{O2 :Ar ratio} * \text{RF Power} + 100.05294 * \text{O2 :Ar ratio} * \text{RF1 bias} - 0.43622 * \text{RF Power} * \text{RF1 bias}$$

$$1.0/(\text{n@633nm}) = +0.47896 + 0.21585 * \text{O2 :Ar ratio}$$

$$\text{Ln(k@633nm)} = +11.25209 - 21.87405 * \text{O2 :Ar ratio} - 0.75347 * \text{Pressure} - 0.11680 * \text{RF Power} + 0.71603 * \text{RF1 bias} - 2.33929 * \text{O2 :Ar ratio} * \text{Pressure} + 0.25293 * \text{O2 :Ar ratio} * \text{RF Power} - 13.45737 * \text{O2 :Ar ratio} * \text{RF1 bias} + 6.79026\text{E-}003 * \text{Pressure} * \text{RF Power} - 0.010910 * \text{RF Power} * \text{RF1 bias} + 0.098354 * \text{O2 :Ar ratio} * \text{RF Power} * \text{RF1 bias}$$

$$[\text{Pb}] = -5.15252 + 17.71069 * \text{O2 :Ar ratio} + 0.092922 * \text{RF Power} + 0.34365 * \text{RF1 bias} - 0.28374 * \text{O2 :Ar ratio} * \text{RF Power} + 3.57606 * \text{O2 :Ar ratio} * \text{RF1 bias} - 7.58598\text{E-}003 * \text{RF Power} * \text{RF1 bias}$$

$$\text{Ln(Ti)} = +1.09901 - 2.93732 * \text{O2 :Ar ratio}$$

$$[\text{Zr}] = -0.12168 + 5.48020 * \text{O2 :Ar ratio} - 0.13771 * \text{Pressure} + 0.025982 * \text{RF Power} + 0.12614 * \text{RF1 bias} - 0.10126 * \text{O2 :Ar ratio} * \text{RF Power} + 1.12925 * \text{O2 :Ar ratio} * \text{RF1 bias} - 1.91314\text{E-}003 * \text{RF Power} * \text{RF1 bias}$$

$$\text{Sqrt}(\text{Pb}/(\text{Ti}+\text{Zr})) = +0.59938 + 3.76765\text{E-}003 * \text{RF Power} - 0.075642 * \text{RF1 bias}$$

The above equations were then used to predict the thickness at various conditions (shown in red box below) and there is good match between the actual and predicted values for film thickness. Refractive index depends only on the oxygen content of the film and absorption coefficient is affected by any plasma variation (Table 3). But these ANOVA models are still useful in predicting the conditions to get high deposition rate PZT thin films without sacrificing its optical properties.

**Table 3:** Validation (top box) and Prediction (bottom box) of optimal operating conditions for a RF sputtering of PZT thin films.

Using these settings in equations on previous slide to predict

			Thickness (t)		Refractive Index (n)		Absorption(k)	
			Actual	Predicted	Actual	Predicted	Actual	Predicted
52/48	3mT/12 Ar/200W	Pt	1410.39	1345.19	2.2758	2.083	8.12E-05	3.40E-05
52/48	3mT/12 Ar/200W + 10W RF1	Pt	708.62	688.7	2.0353	2.083	1.64E-12	1.46E-11
52/48	3mT/12 Ar/200W + 3sccms O2	Pt	918.31	856.58	2.0285	1.89	5.87E-03	0.007673

Constraints							
Name	Goal	Lower Limit	Upper Limit	Lower Weight	Upper Weight	Importance	
O2:Ar ratio	is in range	0	0.5	1	1	3	
Pressure	is in range	3	7	1	1	3	
RF Power	is in range	100	200	1	1	3	
RF1 bias	is in range	0	10	1	1	3	
thickness	maximize	355.04	1369.34	1	1	3	
1.0(n@633nm)	is in range	0.394446	0.620194	1	1	3	
Ln(k@633nm)	minimize	-24.9473	-0.546177	1	1	3	

Solutions								
Number	O2:Ar ratio	Pressure	RF Power	RF1 bias	thickness	1.0(n@633nm)	Ln(k@633nm)	Desirability
1	0.00	3.00	200.00	5.00	1017.02	0.479	-17.612	0.676
2	0.00	3.50	200.00	3.78	1097.11	0.479	-15.533	0.670

Predicted process conditions for above criteria

A 2<sup>nd</sup> DOE was conducted to ensure that we have more robust models around the preferred operating point and the resultant responses are shown in Table 4.

**Table 4:** 2<sup>nd</sup> full factorial statistical design of experiment in 3 process variables and the measured VASE responses.

Std	Run	Block	Factor 1 A:O2 flow sccm	Factor 2 B:RF Power W	Factor 3 C:RF1 bias W	Response 1 thickness A	Response 2 n@633nm	Response 3 k@633nm	
	3	1	Block 1	0.00	200.00	0.00	1179.71	2.3469	0.010492
	7	2	Block 1	0.00	200.00	2.00	1025.72	2.2847	0.0018355
	8	3	Block 1	2.00	200.00	2.00	505.9	2.1958	0.011107
	1	4	Block 1	0.00	150.00	0.00	817.54	2.2963	0.0088137
	6	5	Block 1	2.00	150.00	2.00	256.21	2.2466	0.020467
	9	6	Block 1	1.00	175.00	1.00	556.29	2.0687	0.0097767
	2	7	Block 1	2.00	150.00	0.00	390.71	2.0197	0.044156
	4	8	Block 1	2.00	200.00	0.00	719.63	2.0161	0.0098381
	5	9	Block 1	0.00	150.00	2.00	642.92	2.2615	0.0020284

The results of analysis of variance of VASE data gave us the following models for responses (this time only

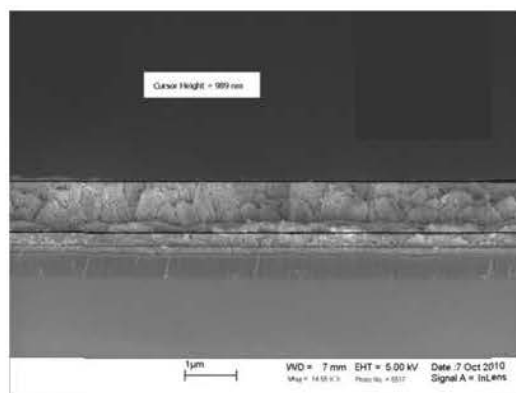
absorption coefficient had to be transformed for more linearity in the model). Noticeably, most of the interaction terms have dropped out of the model. The expected effect of plasma variables on refractive index and absorption coefficient is more evident and realistic.

$$\text{Thickness} = -157.05500 - 224.18000 * \text{O2 flow} + 6.61790 * \text{RF Power} - 84.60500 * \text{RF1 bias}$$

$$n@633\text{nm} = +2.32160 - 0.15185 * \text{O2 flow} - 0.024250 * \text{RF1 bias} + 0.062950 * \text{O2 flow} * \text{RF1 bias}$$

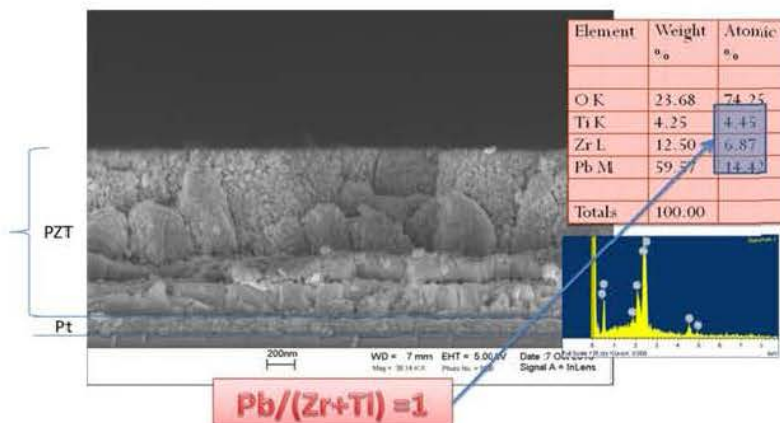
$$1.0/(k@633\text{nm}) = +104.38522 - 21.11945 * \text{O2 flow} + 207.25991 * \text{RF1 bias} - 101.80498 * \text{O2 flow} * \text{RF1 bias}$$

Based on the SDE's, we targeted a 1 micron PZT film with Pb/(Zr+Ti) ratio of 1 and low absorption coefficient. SEM cross-section in Fig. 19 shows a film of 989 nm whilst our VASE measurement was 903nm. The slight discrepancy is due to low magnification of the SEM picture. On careful perusal, one can observe a thin initiation layer. This is a high deposition rate thin layer of 80-100nm PZT that will provide nucleation for creating crack free films.



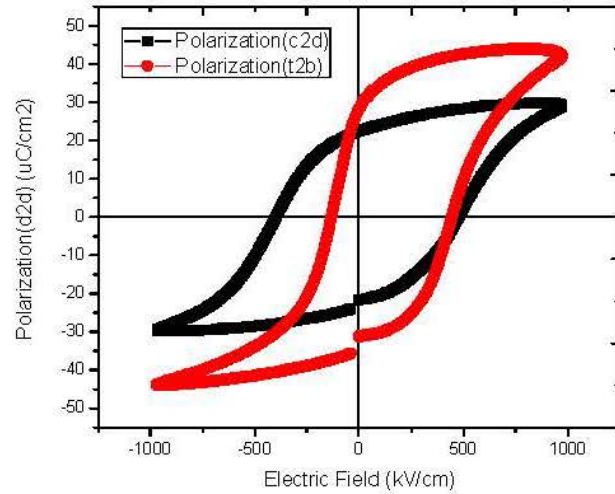
**Figure 19:** SEM cross section of the PZT film over a 260nm sputtered Pt/ 50nm Ti/500nm SiO<sub>2</sub>/Si substrate.

We also conducted an EDX scan of the PZT thin film and evidently as shown in Fig. 20, we did obtain the Pb/(Zr+Ti) ratio of 1. The individual elemental concentrations [Pb], [Zr] and [Ti] were incongruent with the ANOVA models as the EDS analysis equipment and software were dissimilar. Earlier EDX data was quantitative whilst this is qualitative due to the standard less nature of the analysis.



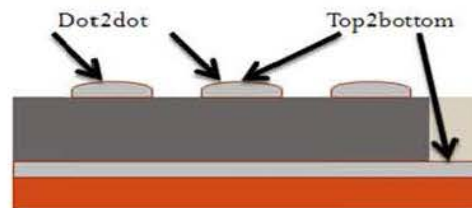
**Figure 20:** EDX stoichiometry results of the PZT film in the blue box.

Figure 21 shows the ferroelectric response of the deposited films exhibiting remnant polarization of  $P_r = 28.04 \mu\text{C}/\text{cm}^2$  and  $22.38 \mu\text{C}/\text{cm}^2$  which is close to that obtained for a sol-gel seed layer textured RF sputtered thin film. The coercive field was  $E_c = 444.7 \text{ kV}/\text{cm}$  &  $475.6 \text{ kV}/\text{cm}$ .



**Figure 21:** Ferroelectric hysteresis loops for  $\sim 0.9 \mu\text{m}$  thick PZT sputtered film.

Two measurements as shown in Fig. 22 were attempted to isolate the effect of substrate clamping – in plane measurement depicted as ‘dot2dot’ and out of plane depicted as ‘top2bottom’. The dot2dot loop is more symmetric due to the lack of residual stress and substrate clamping effects.



**Figure 22:** Test probe configuration for in-plane vs. out-of-plane measurements.

The results of the 2<sup>nd</sup> DOE Analysis of Variance of VASE data gave us the following models for responses:

$$\text{Thickness} = -157.05500 - 224.18000 * \text{O2 flow} + 6.61790 * \text{RF Power} - 84.60500 * \text{RF1 bias}$$

$$\text{n@633nm} = +2.32160 - 0.15185 * \text{O2 flow} - 0.024250 * \text{RF1 bias} + 0.062950 * \text{O2 flow} * \text{RF1 bias}$$

$$\text{1.0/(k@633nm)} = +104.38522 - 21.11945 * \text{O2 flow} + 207.25991 * \text{RF1 bias} - 101.80498 * \text{O2 flow} * \text{RF1 bias}$$

We also conducted EDX scans of the PZT thin films generated by these 2 SDE’s. The ANOVA models for the same are shown below. But we decided to proceed further and investigate a method to correlate the optical properties of these films with the elemental composition (as in Figure 22).

$$\text{[Pb]} = -5.15252 + 17.71069 * \text{O2 :Ar ratio} + 0.092922 * \text{RF Power} + 0.34365 * \text{RF1 bias} - 0.28374 * \text{O2 :Ar ratio} * \text{RF Power} + 3.57606 * \text{O2 :Ar ratio} * \text{RF1 bias} - 7.58598\text{E-}003 * \text{RF Power} * \text{RF1 bias}$$

$$\text{Ln}(\text{Ti}) = +1.09901 - 2.93732 * \text{O2 :Ar ratio}$$

$$[\text{Zr}] = -0.12168 + 5.48020 * \text{O2 :Ar ratio} - 0.13771 * \text{Pressure} + 0.025982 * \text{RF Power} + 0.12614 * \text{RF1 bias} - 0.10126 * \text{O2 :Ar ratio} * \text{RF Power} + 1.12925 * \text{O2 :Ar ratio} * \text{RF1 bias} - 1.91314\text{E-}003 * \text{RF Power} * \text{RF1 bias}$$

$$\text{Sqrt}(\text{Pb}/(\text{Ti}+\text{Zr})) = +0.59938 + 3.76765\text{E-}003 * \text{RF Power} - 0.075642 * \text{RF1 bias}$$

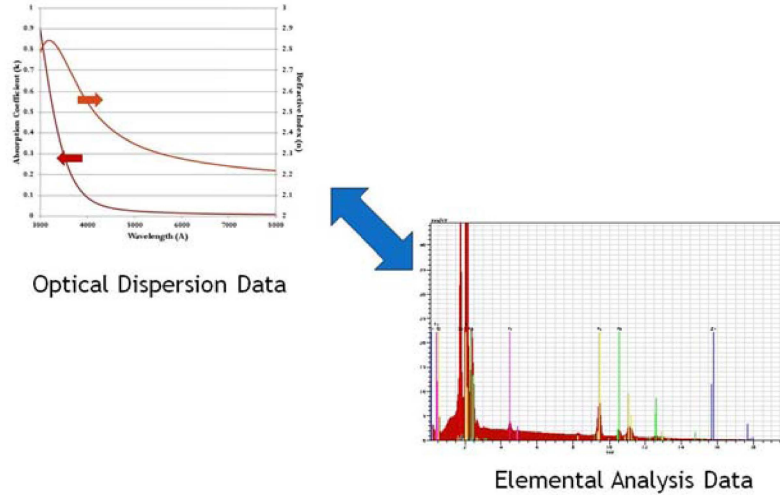


**Figure 22:** Typical Optical properties vs. wavelength for a particular PZT film and its elemental composition as measured by Energy Dispersive X-ray Analysis.

We plotted and computed Tauc and Wemple-DiDomenico parameters from the optical dispersion data (Figure 23). We then regressed any correlation between elemental composition and these parameters. But we needed another parameter to equate with the number of unknowns in the resultant model equations. From Figure 24, electronic polarizability affects the optical properties of a thin film and so we computed it using 3 different approaches (as plotted in Figure 25).

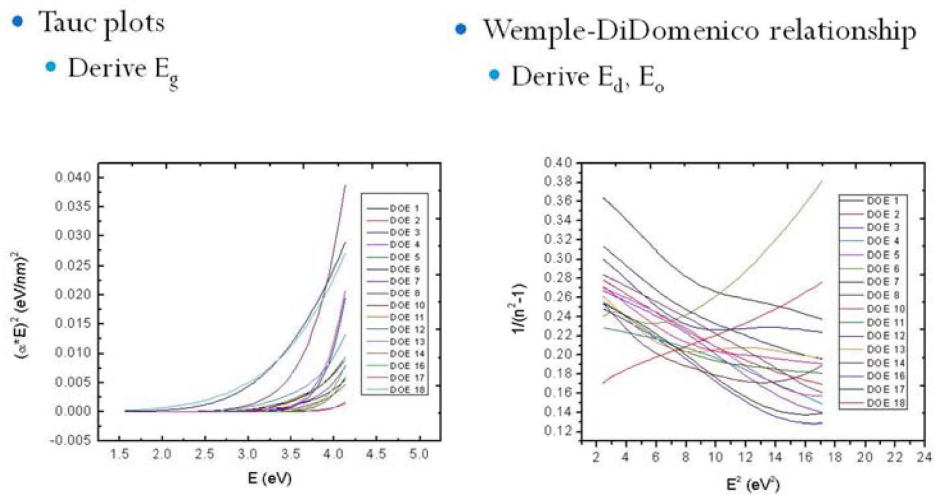


**Figure 23:** Tauc and Wemple-DiDomenico plots for 1<sup>st</sup> SDE PZT thin films.

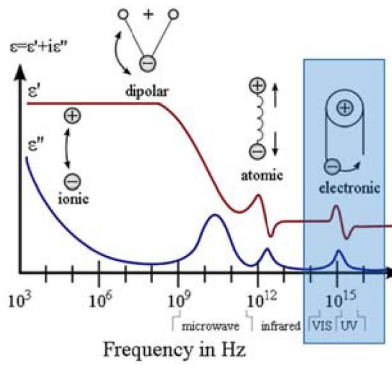


Figure 24: Electronic Polarizability and Optical dielectric response of a thin film

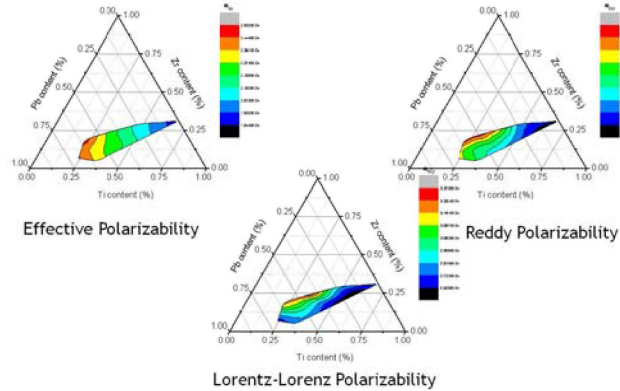


Figure 25: Electronic polarizabilities calculated using 3 different approaches.

Using the Tauc, Wemple-DiDomenico and Polarizability correlations to composition, we can predict the composition of a thin film from the same system by substituting the measured optical dispersion parameters. The model equations for the 1<sup>st</sup> SDE and the model predictions using this methodology are shown below. This methodology translates into a lab scale non-destructive compositional prediction model for multi component thin films.

- Using values for  $E_o$  or  $E_d$  or  $E_g$  from sample and previously derived correlations (shown below), solve for  $f_{Pb}$ ,  $f_{Zr}$ ,  $f_{Ti}$  and  $f_O$

$$t_{f_{PZT}} = \frac{f_{Pb}r_{Pb} + f_O r_O}{\sqrt{2}(f_{Zr}r_{Zr} + f_{Ti}r_{Ti} + f_O r_O)}$$

$$f_{Ti} = -0.132151 + 0.0375312 * E_o$$

$$f_{Zr} = -0.066168 + 0.0193297 * E_o$$

$$f_{Pb} = 0.3855925 - 0.0586112 * E_o$$

$$\alpha_m = -6.59e - 25 + 4.01e - 24 * t_f$$

$$\alpha_{m,r} = 1.821e - 24 + 0.452158 * \alpha_m$$

$$\alpha_{m,r} = 1.348e - 24 + 0.7085994 * \alpha_m$$

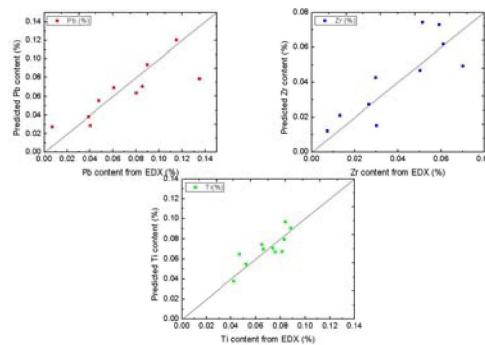
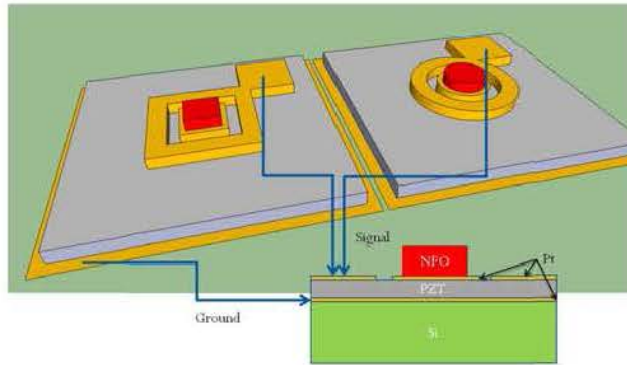


Figure 26: The correlations (left) and the predictability (right) of the new methodology.

### 4.3 Magnetic Field Sensor Fabrication

The single layer transformer structure is shown in Fig. 27. It consists of a nickel ferrite (NFO) dot over a patterned platinum electrode which in turn is over a patterned or un-patterned PZT thin film. A diffusion barrier layer might be incorporated between the PZT and Si so as to prevent  $SiO_2$  formation. It could a layer of

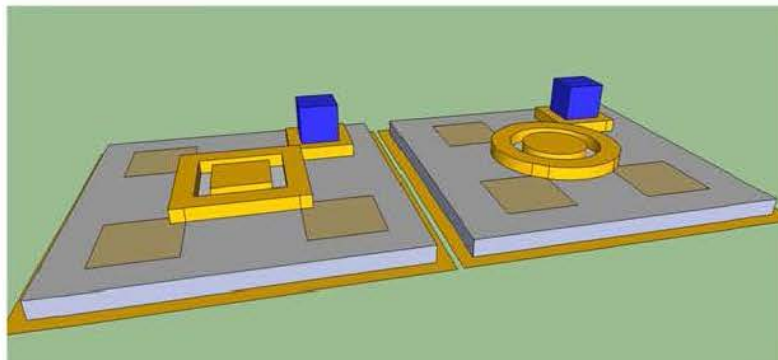
Pt which can serve as the ground for both input (ring) and output (dot) electrodes.



**Figure 27:** Schematic of a single layer transformer-based sensor structure.

We have utilized photo etched metal shadow masks to deposit patterned thin films (see Table below for process sequence). We also used magnets (shown in blue in Figure 28) to protect the underlying layer's electrical pads from deposition.

Process	Mask orientation	Magnets
SiO2 deposition		
Ti deposition		
Blanket bottom Pt deposition		
PZT mask		
PZT deposition		
PZT annealing		
1st Ring pattern/mask		
Pt deposition		
1 Pad protection		1
PZT deposition		1
PZT annealing		
2nd Ring pattern/mask	Rotate90deg	
Pt deposition		
2 Pad protection		2
PZT deposition		2
PZT annealing		
3rd Ring pattern/mask	Rotate90deg	
Pt deposition		
3 Pad protection		3
PZT deposition		3
PZT annealing		
4th Ring pattern/mask	Rotate90deg	
Pt deposition		
4 Pad protection		4
PZT deposition		4
PZT annealing		
Final Ring- Dot pattern/mask		
Pt deposition		



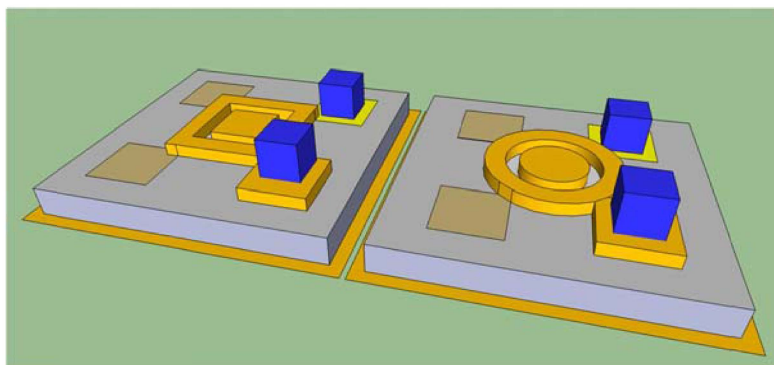


**Figure 28:** Shadow mask processing using metal shadow mask and magnets (to protect electrical pads from deposition).

We had to develop custom testing capability for testing our ME devices. We procured a Agilent E4991A Impedance Analyzer, Jmicro Technology probe station and GGB Picoprobes with special wire tethers (to create common ground between input and output). Figure 29 shows the measurement system.

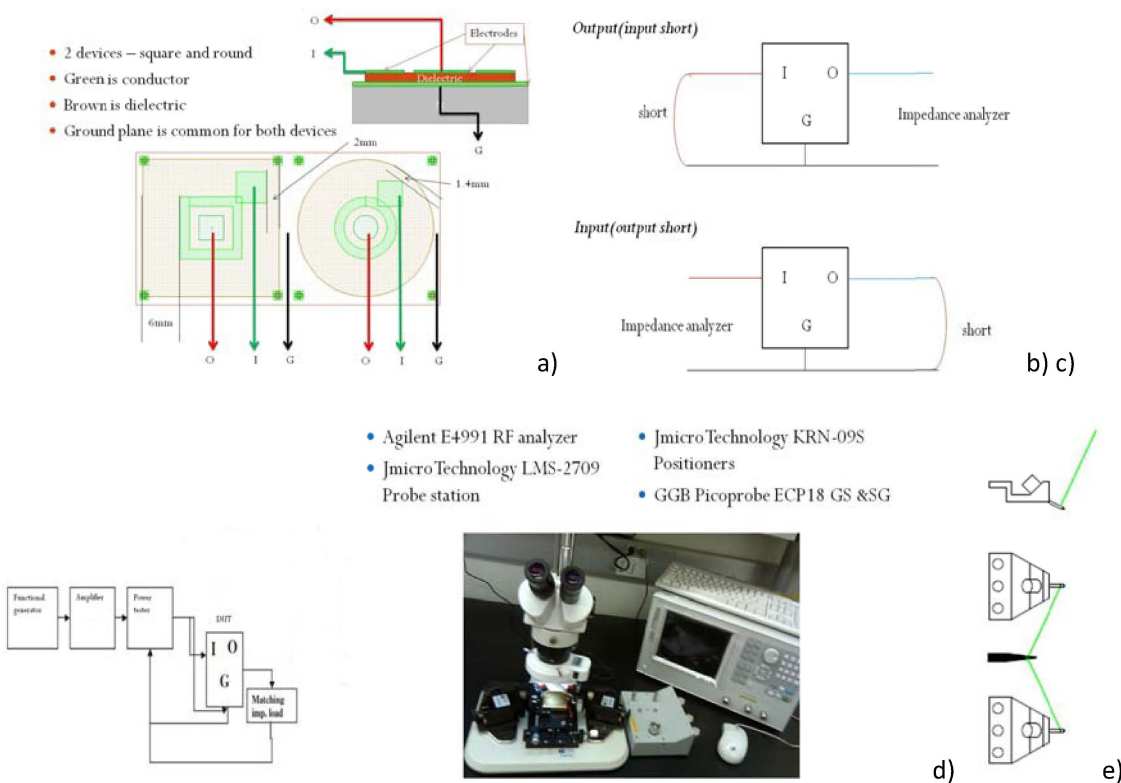


**Figure 29:** Electrical connections and equipment for High Frequency ME testing – a) DUT (device under test), b) impedance testing schematic, c) Gain testing schematic, d) test bench and e) probe tip with special wired tethers for common ground.

We first fabricated the multilayer piezoelectric transformer based on tape-casting technique and low temperature co-firing process. The advantage of this technique is low cost and availability for industry manufacture. With optimized inner electrode composition and co-firing process, we were successful in achieving high density and crack free co-fired PZNT (0.8PZT (52:48)-0.2PZN) multilayer transformer at

930°C. On the co-fired multilayer transformer, we attached two layers of Met-glass on both side of the output section with dimension of  $4 \times 4 \text{ mm}^2$  to fabricate the laminated ME transformer as shown in Fig. 30. With Met-glass attached on the output area, we were able to tune the performance of the transformer under external DC magnetic bias as shown in Fig. 31 and Fig. 32.

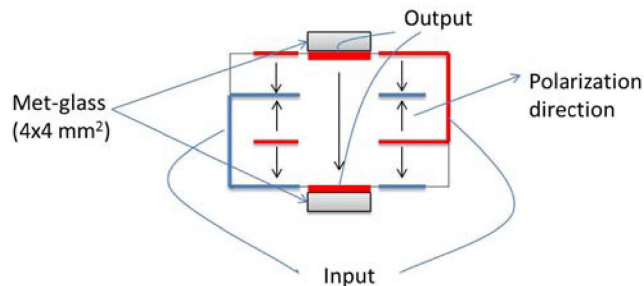


Figure 30: Schematic of ME transformer structure.

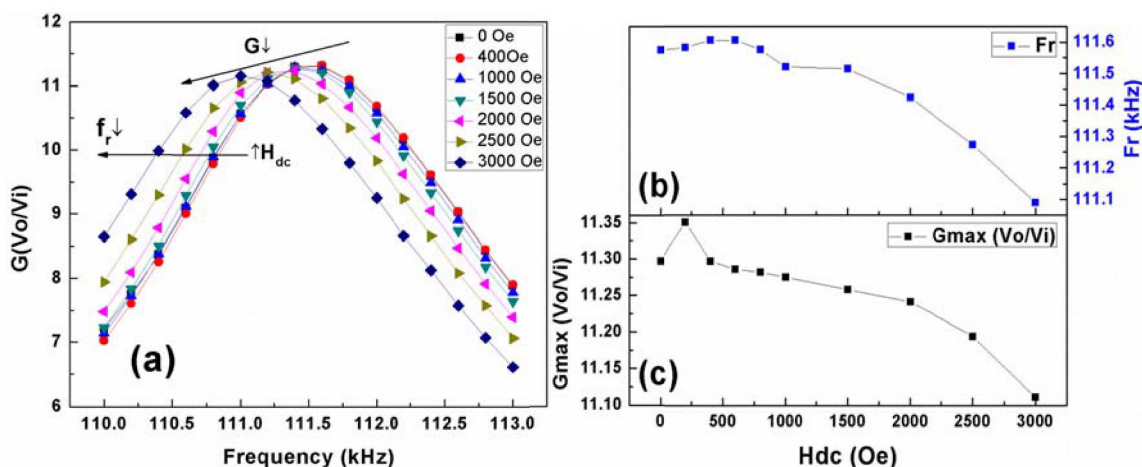


Figure 30: (a) ME transformer voltage gain as a function of frequency at varying external DC magnetic field from 0 Oe to 3000 Oe, (b) Variation of resonance frequency as a function of external DC magnetic field, (c) Change in maximum voltage gain with respect to change in the DC magnetic field.

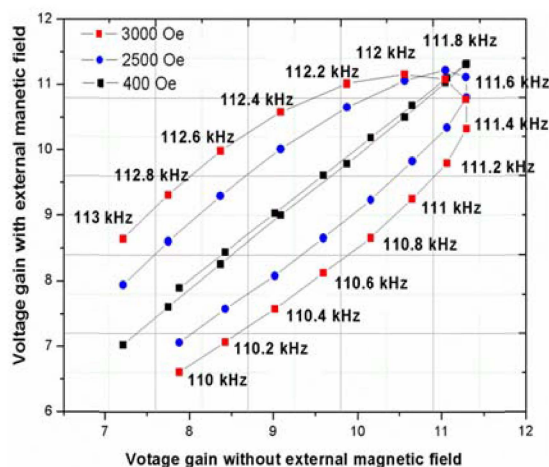
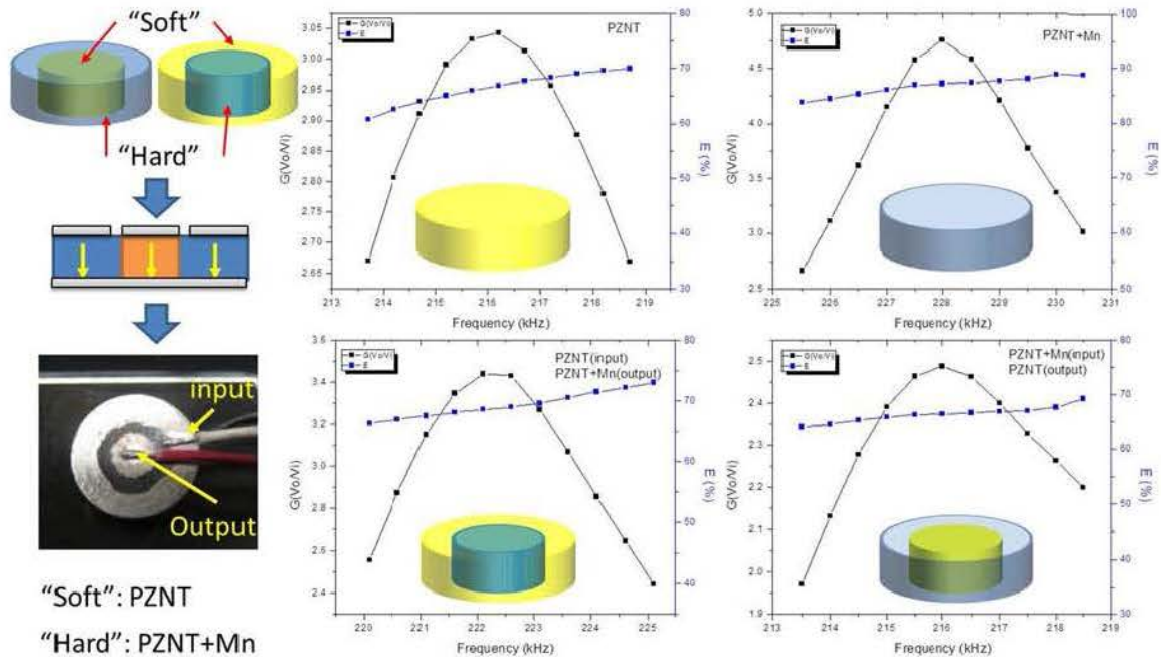


Figure 31: ME transformer characterization showing the change of voltage gain in the frequency range of 110 kHz~113 kHz with and without applied DC magnetic field.

When the transformer was operated under external magnetic field range of 400 Oe to 3000 Oe, the value of maximum voltage gain and its working frequency were found to increase first with increasing  $H_{dc}$  and then decrease with increasing  $H_{dc}$ . Also, we can notice that the voltage gain tunability ( $G_H - G_0 / G_0$ ) of the transformer is small at low magnetic field below 1000 Oe but increased at high magnetic field. The trend of resonance frequency shift was found to be as expected from the equivalent circuit models. The data clearly demonstrates our hypothesis of tunable performance of ME transformer under external magnetic field.

**Graded transformer:** Since the piezoelectric transformer can be seen as a combination of actuator (input) and transducer (output), we experimented with a new transformer structure with different materials at input and output section. Materials which possess higher  $d_{33}$  are suitable for actuator and those with higher  $Q_m$  are suitable as a transducer. This design provides the potential of achieving better performance and new structure of ME tunable transformer. Figure 32 shows the structure of graded transformer. This figure shows comparison of voltage gain and efficiency performance between single phase piezoelectric transformer and graded transformer. Further analysis has to be conducted on this new design with aim of improving piezoelectric transformer performance.



**Figure 32:** Graded piezoelectric transformer with ring-dot structure.

#### 4.4 Hybrid deposition process

We developed hybrid deposition process to achieve high quality films by combining pulsed laser deposition (PLD) and sol-gel. Pulsed laser deposition has high deposition rate and flexibility in target material but as-deposited films are not well textured. So by taking the advantage of orientation control in sol-gel process and high deposition rate of PLD process, we expect to achieve high quality textured film. The sol preparation, gelation process and perovskite crystallization process were optimized for (100) orientation. Pulsed laser deposition with parameter (9E-4 Torr ambient oxygen pressure, 90 min, room temperature) was

conducted. Film were grown at room temperature on as deposited PZT seed layer (sol-gel). In-situ annealing temperature was varied in the range of 250°C to 650°C. Crystallization was determined by using X-ray diffraction (XRD) as shown in Fig. 33. We can notice that this process provides  $\langle 100 \rangle$  preferred orientation. The fraction of texturing increased 20% from 58.7% (seed layer) to 79.12% (2<sup>nd</sup> deposited film) by using this hybrid process.

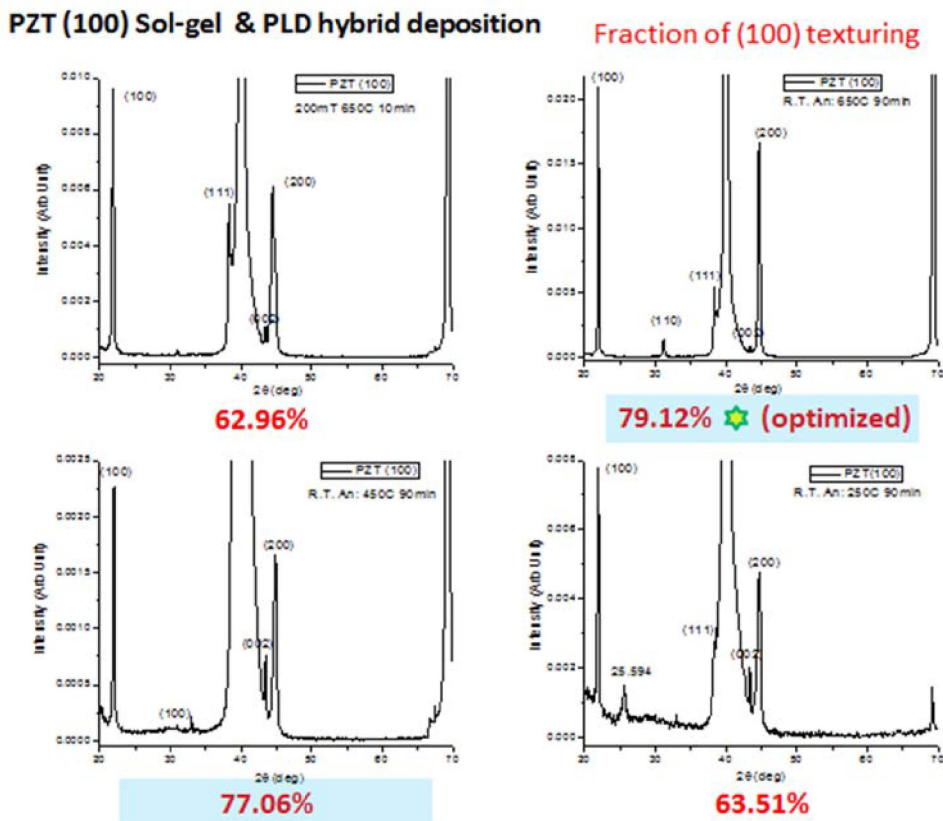


**Figure 33:** XRD pattern of  $\langle 100 \rangle$  textured PZT film on platinized Si via hybrid deposition.

Using the films deposited through this combinatory process, we started to fabricate the unipoled transformer structure. Figure 34 shows a series of image of the first prototype. Ring-dot silver electrode was printed by aerosol jet deposition system. Further investigation on voltage gain will be conducted in the near future.

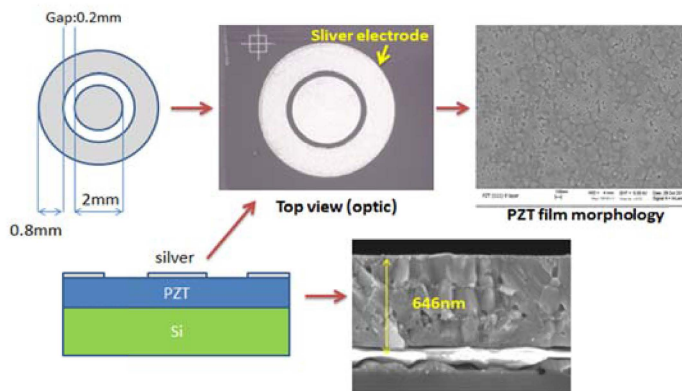


**Figure 34:** Unipoled PZT thin film transformer.

Figure 35 shows the developed hybrid deposition process by combining pulsed laser deposition (PLD) and sol-gel. High deposition rate can be achieved by this process for thick film growth. In addition, high fraction of texture can be obtained via optimized deposition parameter.

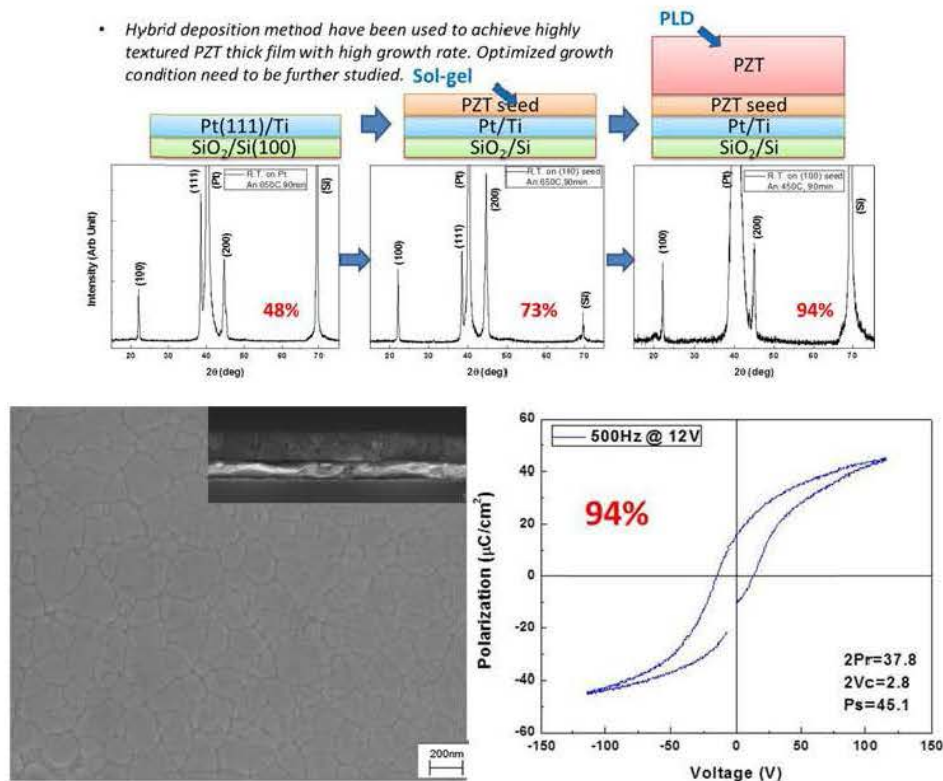


**Figure 35:** Schematic of hybrid deposition process, XRD evolution of hybrid deposited PZT films under varied annealing temperature, microstructure and piezoelectric properties of (100) highly textured  $Pb(Zr_{0.6}Ti_{0.4})O_3$  thick film.

#### Hetero-structure growth of $BaTiO_3$ (BTO) & $CoFe_2O_4$ (CFO)

We studied the growth and microstructure of  $BaTiO_3$  (BTO) thick films on platinized silicon substrate synthesized by pulsed laser deposition as shown in Fig. 36. We investigated the evolution of microstructure and piezoelectric response for as-grown BTO film as a function of thickness. Interestingly, the surface morphology of the films adopted the symmetry of underlying layer and evolved from pyramid to hexagram shape columnar structure with (111)-preferred orientation as the film thickness was increased. The piezoelectric properties were also found to increase with thickness. We expect that the structure-property relationship described for the thick BTO piezoelectric film in this study will strengthen the integration of BTO with silicon.

For thin film ME tunable transformer, it is advantageous to study the magnetoelectric heterostructure that offers the potential of magnetic or electric field induced tunability. We have not only developed conventional 2-2 type structure to study the interaction between two different phases, but also created a new magnetoelectric structure which might possess better performance on ME coupling. Figure 37 shows TEM image of ion bombardment assisted as-grown  $BaTiO_3/CoFe_2O_4$  heterostructure and its ferroelectric properties.

Ion bombardment induced defect were found as a result of merged columnar structure which could provide us a new method to tune ferroelectric properties via modulation of defect density.

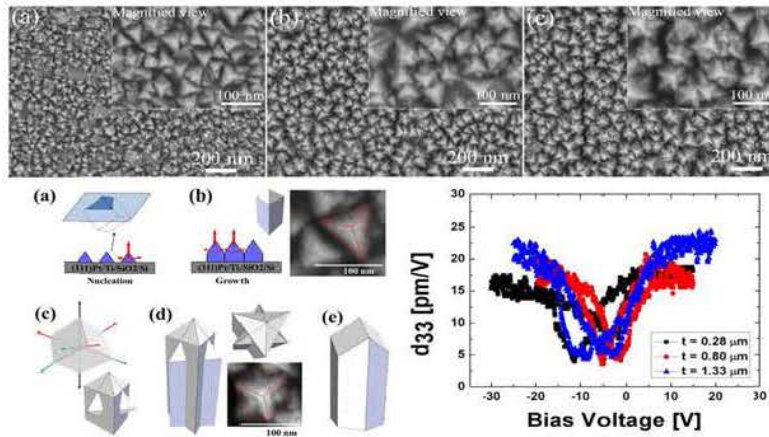


**Figure 36:** Morphology evolution and piezoelectric properties of as-grown BaTiO<sub>3</sub> thick film.

The interaction between these two phases was studied with varying deposition temperature and BTO thickness. Deposition parameter for single layer BTO and CFO film was optimized as 100mTorr ambient oxygen pressure and deposition temperature of 700-850°C. Further study on effect of variables such as BTO thickness and growth temperature was conducted as shown in Fig. 38. Grain size and thickness were found to be quite sensitive to the BTO thickness and growth temperature. Triangular topology was found to dominate grain shape SEM which reflect film growth on (111) oriented Pt as shown in Fig. 39.

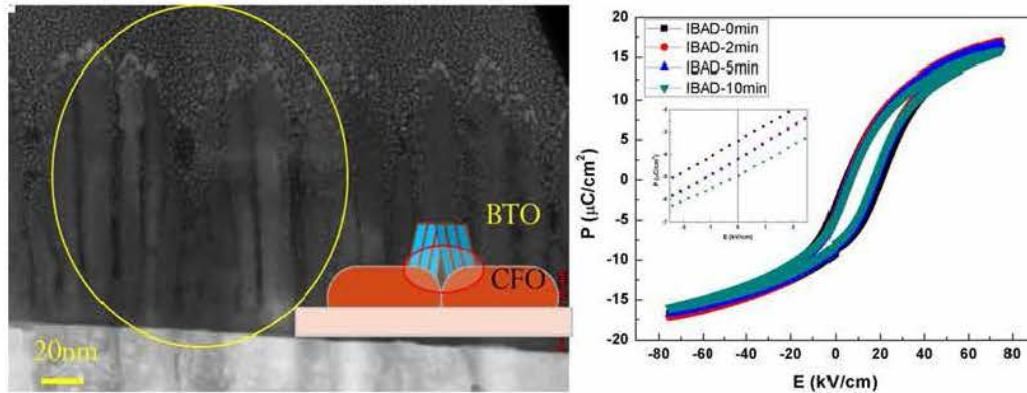


**Figure 37:** TEM image and ferroelectric properties of as grown BaTiO<sub>3</sub>/CoFe<sub>2</sub>O<sub>4</sub> heterostructure.

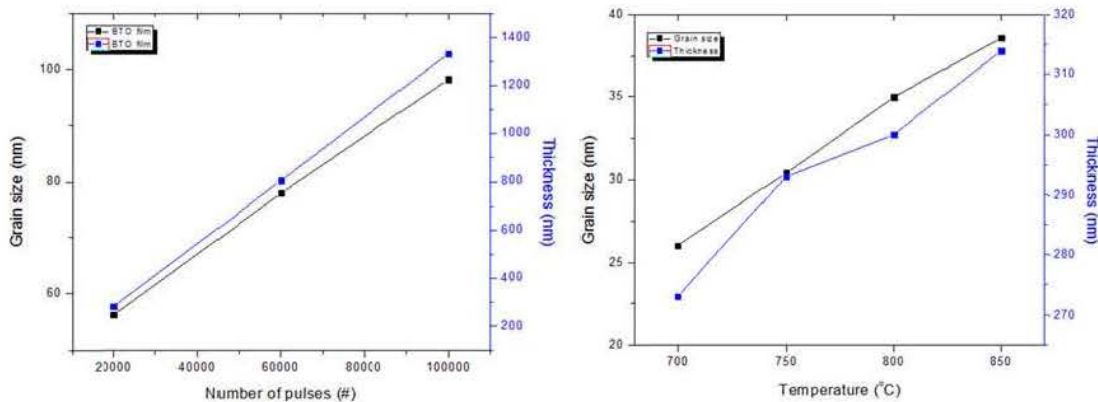


**Figure 38:** Effect of thickness and temperature variable during heterostructure growth.

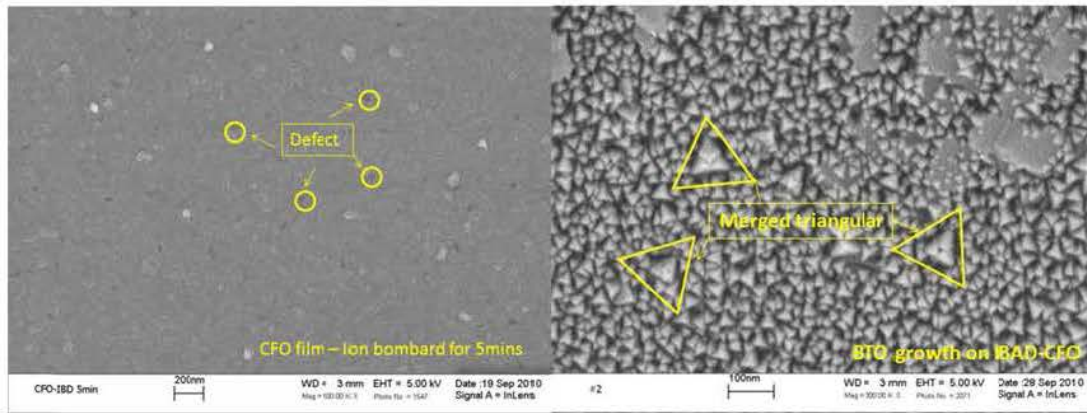


**Figure 39:** SEM image of IBAD-CFO(left) and BTO on as-grown IBAD-CFO film.

We have quantified magnetization and polarization as a function of ion bombardment time as shown in Fig. 40. As expected, saturation magnetization decreased with increasing ion bombardment time. The reason for this trend was related to decrease in CFO film thickness with increase in ion bombard time. P-E loop in this heterostructure shows better hysteresis than simply BTO/CFO and BTO films. The reason for this change still under investigation. We also measured ferroelectric properties change as a function of magnetic field as shown in Fig. 41. We can clearly notice the variation of ramanent polarization change which demonstrates the existence of coupling between magnetic and ferroelectric components.

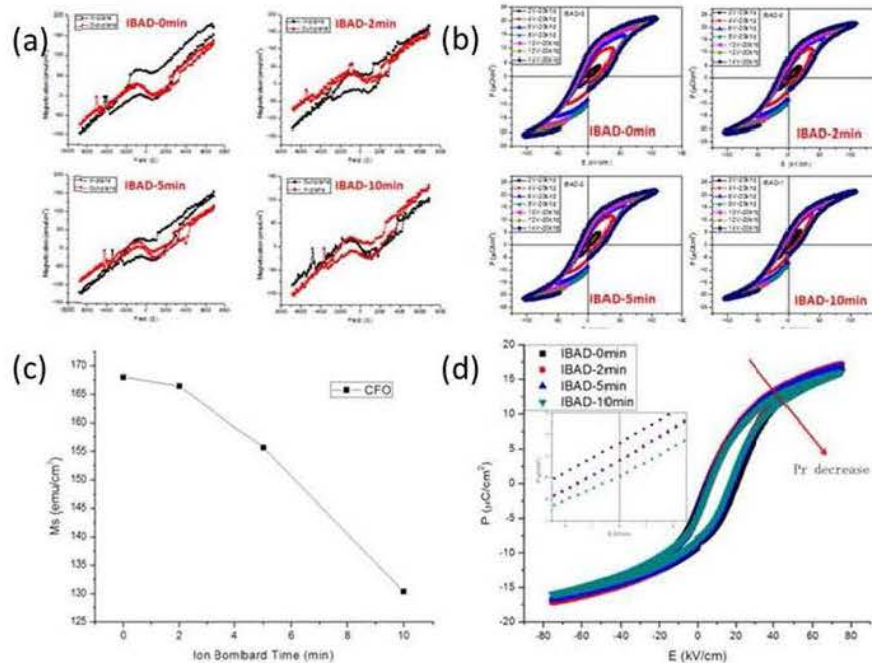


**Figure 40:** (a) M-H loop of IBAD-CFO films; (b) P-E loop of BTO/IBAD-CFO films; (c) Comparison of magnetization of IBAD-CFO film and (d) Comparison of ferroelectricity as a function of Ion-bombardment time.

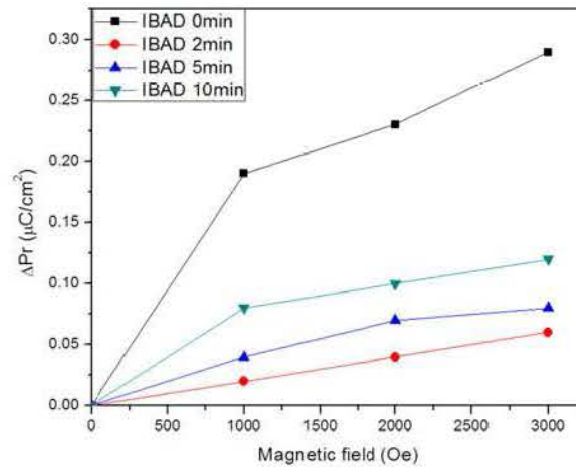


**Figure 41:** Ramanent polarization change as a function of magnetic field for as-grown IBAD heterostructures.

### Complex 3D ME composites

In order to break the conventional phase connectivity, we investigated novel composite structures that can overcome the limitations imposed by material symmetry as shown in Fig. 42. In this process, we start with a pattern deposited by aerosol deposition (AD) on a platinized silicon substrate and then use pulsed laser deposition (PLD) to grow multilayers of BaTiO<sub>3</sub> and CoFe<sub>2</sub>O<sub>4</sub>. After in-situ annealing at high temperatures, the deposited films self-assemble into complex structures. Lastly, we use sol-gel to achieve homogeneous top surface. A combination of these three techniques can be used to fabricate large-area arrays of magnetoelectric structures. This synthesis method not only helps in achieving a well-ordered arrangement of the nanoscale magnetoelectric structures but also simplifies the classical top-down patterning and multi-step processing. We have been focusing on synthesis of these structures and further would like to conduct detailed investigation on understanding of their static and dynamic ferroelectric and ferromagnetic behavior at nanometer scale, ferroelastic domain structures, and magnetoelectric coupling.

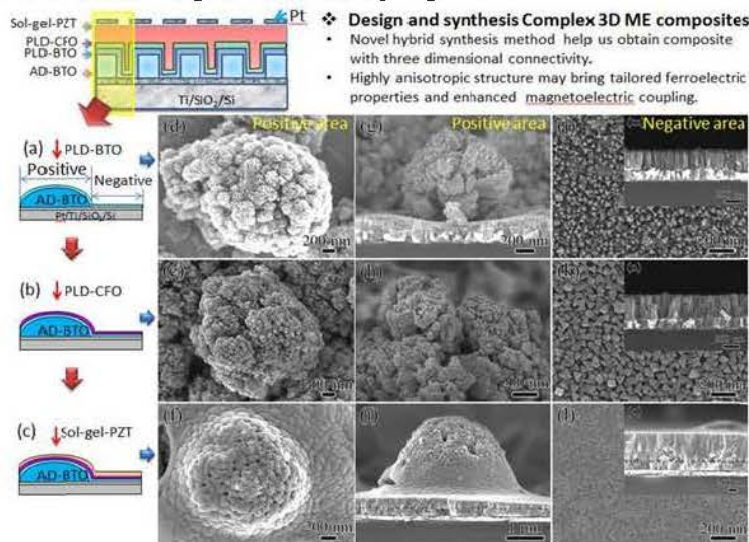


**Figure 42:** Design and synthesis of complex 3D ME composites.

Using this process, we designed and synthesized a new structure of CFO/PZT ME composite array with multi-orientation as shown in Fig. 43. With highly textured buffered array pattern (aerosol jet deposited PZT) and optimized growth condition of CFO/PZT heterostructure, we successfully obtained composite array with multiorientation. CFO inside the pattern shows highly (111) preferred orientation while outside the pattern shows highly (100) preferred orientation with smaller grain size.

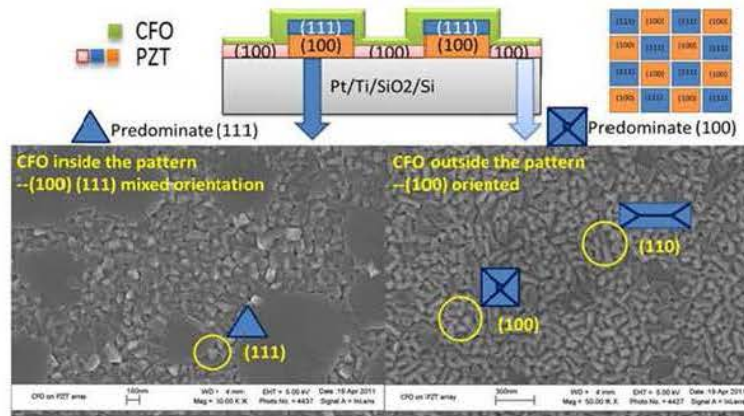


**Figure 43:** CFO/ PZT ME composite array with multi-orientation.

Interestingly, MFM image of as grown film shows different magnetic response closely related with grain size and orientation at different area of the array. CFO with larger grains possesses larger magnetic response, while small grains possess relative smaller response. The reason for the response variation might be grain size and orientation difference. This provide us the information that we might be able to tune magnetic response by modifying grain size and orientation during heterogeneous growth. Moreover, we can observe higher piezoreponse on small CFO grains which show relative small magnetic response inside the pattern. This might be explained through magnetoelectric coupling. With applied bias voltage, PZT film below will transfer strain to the magnetic layer which in return shows high piezoreponse amplitude on the surface.

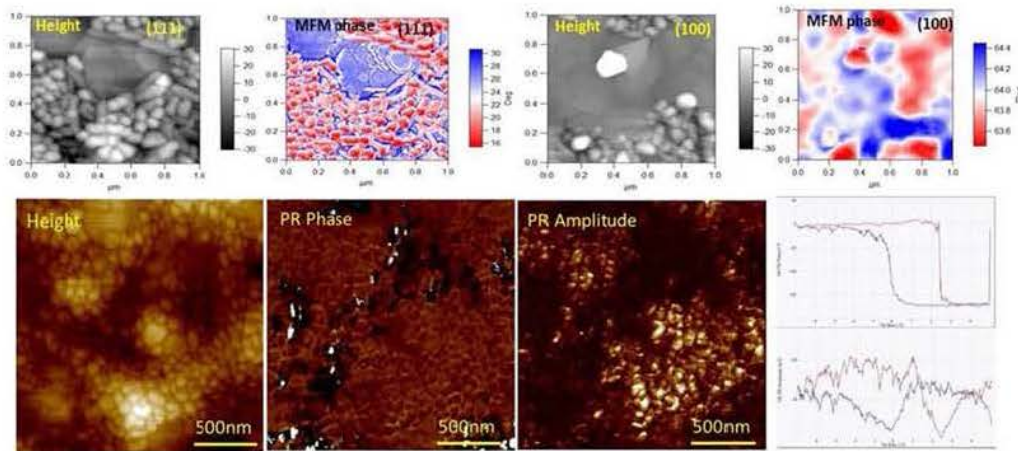


**Figure 44:** Magnetic force microscopy (MFM) images and Piezoresponse force microscopy (PFM) images of as grown film.

### Conclusions

We have developed textured PZT thin films using two different deposition techniques, sol-gel and RF sputtering. We have characterized these films for their composition, structure and crystallinity. An upshot of

the detailed characterization was the development of prediction models for texturing of PZT sol-gel thin films, an understanding of the analytical techniques that can discriminate between the highly textured films, optimization of the RF sputtered PZT thin film properties using design of experiments methodology and finally the establishment of a lab scale non-destructive compositional analysis methodology for PZT RF sputtered thin films using Ellipsometry. We have conceived a unipoled thin film transformer device utilizing the existing toolset at VT's MicrON clean room facility (for mask alignment) and our sputtering capability. We have fabricated single layer transformer structure and characterized its performance.

## References

1. Chee-Sung Park et.al. –“Orientation control of lead zirconate titanate film by combination of sol-gel and sputtering deposition”, Journal of Materials Research - Vol. 20, No. 1, Pages: 243-246, Jan 2005
2. Chen, San-Yuan; Chen, I-Wei (1994). "Temperature–Time Texture Transition of Pb(Zr 1– x Ti x )O 3 Thin Films: I, Role of Pb-rich Intermediate Phases“; Journal of the American Ceramic Society 77(9): 2332-2336.
3. Sadao Adachi, “Optical Properties of Crystalline and Amorphous Semiconductors: Materials and Fundamental Principles”; Kluwer Academic Publishers, 1999.

## **5. A list of papers (already published, in press, submitted) in which AFOSR support is acknowledged.**

### Conferences:

1. R. Varghese, S. Gupta, S. Priya, “Role of Thermal and Chemical treatments on Crystalline Orientation and Optical properties of PZT thin films”, 7th International Workshop on Piezoelectric Materials and Applications in Actuators, October 13<sup>th</sup> 2010, Antalya, Turkey.
2. R. Varghese, S. Priya, “Texturing, Piezoelectric Properties, and Device Integration of Sputtered PZT thin films”, MS&T 2010, October 20<sup>th</sup> 2010, Houston, Texas (USA).
3. (IWMPA-6-A-52-2010), 7th International workshop on piezoelectric materials and applications in actuators, “Growth and microstructure of Pulsed laser deposition of BTO Thin films on Aerosol Jet printed substrates”, Y. Zhou, C. Folgar, Y. Yan, S.Priya.
4. (EMA-S2-039-2011), Electronic Materials and Application, “Ion-assisted Growth of BaTiO<sub>3</sub>/CoFe<sub>2</sub>O<sub>4</sub> Heterostructures in Pulsed Laser Deposited.”, Y. Zhou, C.-S. Park and S. Priya.
5. EMA-S4-005-2010. Co-fired Magnetoelectric Laminate Composite. *C. Park; C. Ahn; S. Priya*; Electronic Materials and Applications 2010, Orlando, Florida, Jan 20 - 22.
6. EMA-S4-010-2010. Broad/Wide Band Magnetoelectric Sensor: Current State and Challenges. *C. Park; C. Ahn; S. Yang; S. Priya*; Electronic Materials and Applications 2010, Orlando, Florida, Jan 20 - 22.
7. EMA-S4-009-2010. Metal – Ceramic Magnetoelectric Composite Gradiometer. *V. Bedekar; Y. Pukinskii; M. Bichurin; D. Viehland; S. Priya*; Electronic Materials and Applications 2010, Orlando, Florida, Jan 20 - 22.
8. R. Varghese, Shashank Priya, “PZT thin film growth and characterization”, CIMSS 2010
9. R. Varghese, Greg Pribil, Shashank Priya, “Lab Scale Non-Destructive Compositional Analysis of PZT RF Sputtered Thin Films”, Materials Science &Technology, October 16-20, 2011

### **Journal Publications**

1. G. Singh, S. Priya, Maria H, S. R. Shah, S. Grover, A Koyman and R. L. Mahajan, “Synthesis, Electrical and Magnetic Characterization of Core-Shell Silicon Carbo Nitride Coated Carbon Nanotubes”, *Mater. Lett.* 63, 2435-2438 (2009).
2. S. Priya, J. Ryu, C.-S. Park, J. Oliver, J.-J. Choi and D.-S. Park, “Piezoelectric and Magnetolectric Thick Films for Fabricating Power Sources in Wireless Sensor Nodes”, *Sensors* 9, 6362 (2009).
3. V. Bedekar, M. Bichurin, S. Ivano, Y. Pukinski, S. Priya, “Metal-ceramic laminate composite magnetolectric gradiometer”, *Rev. Scientific Instr.* 81, 033906 (2010).
4. V. Bedekar, M. Murayama, R. L. Mahajan, and S. Priya, “Controlled Synthesis of BaTiO<sub>3</sub>-Coated Multiwall Carbon Nanotubes”, *J. Amer. Ceram. Soc.* 93, 3618 – 3623 (2010).
5. R. Varghese, S. Gupta, S. Priya, “Temperature-time transformation diagram for Pb(Zr,Ti)O<sub>3</sub> thin films”, *J. Appl. Phys.* 110, 014109 (2011); doi:10.1063/1.3606433

### **Patent Disclosures**

1. Ronnie Varghese and Shashank Priya, VTIP 11-136 – “Copper Direct Write Process with Corrosion Inhibitor”.
2. Ronnie Varghese and Shashank Priya, PZT Thin Films for MEMS by RF Sputtering: Optimization of Optical and Electrical Performance

### **Journal Papers (to be submitted)**

1. “Microstructure evolution and ferroelectric properties of pulsed laser deposited BaTiO<sub>3</sub> thick films”, Yuan Zhou, Chee-Sung Park, Ashok Kumar, R. S. Katiyar and Shashank Priya, *J. Appl. Phys.* (April 2012)
2. “Tunable magnetolectric multilayer transformer”, Yuan Zhou, Chee-Sung Park and Shashank Priya, *J. Appl. Phys.* (March 2012).
3. “Lab scale non-destructive compositional analysis of PZT RF sputtered thin films using Spectroscopic Ellipsometry”, Ronnie Varghese, Bill Reynolds, and Shashank Priya, *Phys. Rev. B* (March 2012).